Facile Fabrication of Robust Hydrogen Evolution Electrodes under High Current Densities *via* Pt@Cu Interactions

Yeshu Tan[1], Ruikuan Xie[2], Siyu Zhao[1], Xuekun Lu[3], Longxiang Liu[1], Fangjia Zhao[1], Chunzhong Li[4], Hao Jiang[4*], Guoliang Chai[2], Dan J.L. Brett[3], Paul R. Shearing[3], Guanjie He[1,3,5*], and Ivan P. Parkin[1*]

[1]*Christopher Ingold Laboratory, Department of Chemistry, University College London, 20 Gordon Street, London WC1H 0AJ, United Kingdom. Email: g.he@ucl.ac.uk; i.p.parkin@ucl.ac.uk*

[2]*State Key Laboratory of Structural Chemistry, Fujian Institute of Research on the Structure of Matter, Chinese Academy of Sciences (CAS), Fuzhou, 350002 Fujian, P. R. China.*

[3]*Electrochemical Innovation Lab, Department of Chemical Engineering, University College London, London WC1E 7JE, United Kingdom.*

[4]*Key Laboratory for Ultrafine Materials of Ministry of Education, Shanghai Engineering Research Center of Hierarchical Nanomaterials, School of Materials Science and Engineering, East China University of Science & Technology, 130 Meilong Road, Shanghai 200237, China. Email: jianghao@ecust.edu.cn*

[5]*School of Chemistry, University of Lincoln, Joseph Banks Laboratories, Green Lane, Lincoln, LN6 7DL, United Kingdom.*

Abstract

Durable and efficient hydrogen evolution reaction (HER) electrocatalysts that can satisfy industrial requirements need to be developed. Platinum (Pt)-based catalysts represent the benchmark performance but are less studied for HER under high current densities in neutral electrolytes due to their high cost, poor stability and extra water dissociation step. Here we propose a facile and low-temperature synthesis for constructing 'blackberry-shaped' Pt nanocrystals on copper (Cu) foams with low loading as self-standing electrodes for HER in neutral media. Optimized hydrogen adsorption free energy ($\Delta G_{*\mathrm{H}}$) and robust interaction induced by charge density exchange between Pt and Cu ensure the efficient and robust HER, especially under high current densities, which are demonstrated from both experimental and theoretical approaches. The electrode exhibits small overpotentials of 35 and 438 mV to reach current densities of -10 and -1000 mA cm^{-2}, respectively. Meanwhile the electrode illustrates outstanding stability during chronoamperometry measurement under high current densities (-100 ~ -400 mA cm^{-2}) and 1000 cycles linear sweep voltammetry tests reaching -1000 mA cm^{-2}. This study provides new design strategies for self-standing electrocatalysts by fabricating robust metal-metal interactions between active materials and current collectors, thus facilitating the stable function of electrodes for HER under technologically relevant high current densities.

Keywords: Hydrogen evolution; High current density; Pt nanocrystals; Self-standing; Pt@Cu interaction

1. Introduction

With increasing energy consumption and rising concerns with environmental pollution, hydrogen as clean and renewable energy has raised great attention for direct use in energy conversion systems, such as proton-exchange membrane fuel cells.[1] Electrochemical water splitting to produce high purity hydrogen has been regarded as an efficient and sustainable process for clean energy generation.[2] The hydrogen evolution reaction (HER) can be performed in acidic, basic or neutral media and platinum (Pt) has been considered as the most effective electrocatalyst in acidic media for HER, owing to its conducive hydrogen adsorption free energy.[3] However, Pt shows undesirable activity when used in neutral media, attributed to sluggish kinetics. Water electrolysis in neutral electrolytes is slower compared with that in acid with an extra water dissociation step.[4] Efficient electrochemical water splitting in neutral media widens the feasibility to produce H_2 in environmental-friendly media, such as using seawater without adding extra alkalis or acids.[5] The cost of certain electrolytes is reduced if seawater and other abundant water resources (for example, domestic waste-water) could be applied in the future. Thus, water electrolysis in a neutral environment has gained much attention and different types of electrocatalysts have been developed.[6] Electrocatalysts such as FeP[7], MoP[8] and SiO_2–polypyrrole[9], have been further studied for HER in neutral media and shows good performance under reasonable current densities, but the development of suitable electrocatalysts to boost the performance is needed to meet the requirements of practical applications under high current densities, making the interaction between electrocatalysts and substrates much

more critical. However, this area is much less explored.

The aggregation and dissolution of electrocatalysts are inevitable problems under working conditions. One of the promising strategies is the construction of a self-standing electrode.[10] Among these, Pt-based self-standing electrodes are major research topics. Based on an atomic layer deposition method (ALD), Pt was deposited directly on laser scribed graphene (LSG).[11] The as-prepared Pt/LSG showed efficient HER performance and excellent durability under a current density of -10 mA cm^{-2}, but the investigation under high current density was not carried out. Additionally, an ultrafine PtCo alloy nanoparticle decorated Co nanowire was developed. The synergistic effects of the heterostructure indicated unprecedented HER performance in alkaline media.[12] Many works focus on the synergetic effect of electrocatalyst with heterostructures, which leads to enhanced electrocatalytic performance.[13] For practical use, the formation of a strong interface between substrates and active species is quite significant, which can ensure the structural stability during fierce H_2 evolution at a high current density; however, it is often ignored because of the high performance under low overpotentials. Recently, Thomas and his co-workers reported the molybdenum carbide nanoparticles as an efficient electrocatalyst under -100 mA cm^{-2} for durability test.[14] Moreover, NiCo@C-NiCoMo/NF was developed by Yin's group, the chronoamperometry measurement was under -1000 mA cm^{-2}, indicating its remarkable stability.[15] On the other side, the robust interaction between electrocatalysts and substrates ensures efficient usage and reduces the loading of active materials.

Most reported Pt-based self-standing electrodes need strict conditions and high

temperatures to fabricate; developing an easy manufacturing process and large-scale Pt-based self-standing electrodes is considered an urgent need. Here, we propose a facile synthetic method to assemble blackberry-shaped Pt nanocrystals with small loading amounts on different metal foams directly. The low Pt loading on Cu foams shows high activity for HER in neutral media because of the optimized hydrogen adsorption free energy (ΔG_{*H}) of Pt@Cu. Meanwhile, Pt@Cu exhibits efficient water dissociation and the small amount of $Cu(OH)_2$ on Cu foams has a strong hydroxide binding energy that can easily adsorb hydroxide in neutral media, thus further facilitating the water dissociation process.[16] The as-prepared Pt@Cu foams show remarkable activities compared with commercial 20% Pt/C materials. Specifically, the self-standing Pt@Cu electrode delivers small overpotentials of 35 and 438 mV to reach current densities of -10 and -1000 mA cm^{-2}, respectively in neutral media. The robust interaction between Pt and Cu ensures the outstanding durability for 1000 cycles LSV tests reaching -1000 mA cm^{-2}, and shows no decay of performance for chronoamperometry measurement under high current densities of -100 to -400 mA cm^{-2} with fierce H_2 bubble production compared with powdery Pt/C electrocatalysts pasted on current collectors.

2. Results and discussion

2.1 Synthesis of blackberry-shaped Pt nanocrystals

Pt nanocrystals are widely applied in HER due to their high activity.[8, 17] Dendritic nanostructures typically exhibit enhanced electrocatalytic performance due to their rough surface morphology.[18] In this work, we use a simple reduction solvent to

synthesize blackberry-like Pt nanocrystals. Surfactant and reduction solvent are modified to propose an easy way to fabricate blackberry-shaped Pt nanocrystals under 50 °C. The X-ray diffraction (XRD) pattern, **Figure 1a,** illustrates its cubic structure, the peak located at 2θ of 18.03° corresponds to the standard Pt (111) lattice plane. The particle size and detailed morphology information of the Pt nanocrystals are shown by scanning electron microscopy (SEM) in **Figure 1b** and transmission electron microscopy (TEM) in **Figure 1c**. The Pt nanocrystals show blackberry-like shapes with an average diameter of ~30 nm and high roughness, leading to more exposure of active sites on the surface. The high-resolution TEM image (HRTEM) in **Figure 1d** indicates a lattice spacing of 2.26 Å, corresponding to the (111) lattice plane of Pt. Ammonium citrate dibasic was used as the surfactant, which helps to form small particles and slow down the reaction on the surface during the reduction process.[19] To make a comparison, polyvinyl pyrrolidone (PVP) was used as another surfactant. SEM images in **Figure S1** illustrate the structural differences with and without the surfactant. Pt nanocrystals with ammonium citrate dibasic show smaller particle size, leading to larger exposed surface area. Pt nanocrystals with PVP indicated the smooth shape and relatively larger size, which is not suitable for dispersion of individual nanocrystal. Different surfactants have unique effects on the crystallization process.

It is found that the solvent plays a key role in the reduction synthesis. Here, hydrazine and L-ascorbic acid were used as different reduction solvents to modify the synthesis. Hydrazine can facilitate the formation of Pt nanocrystals under room temperature, but the fast reduction process leads to the growth of larger particles and irregular shapes as
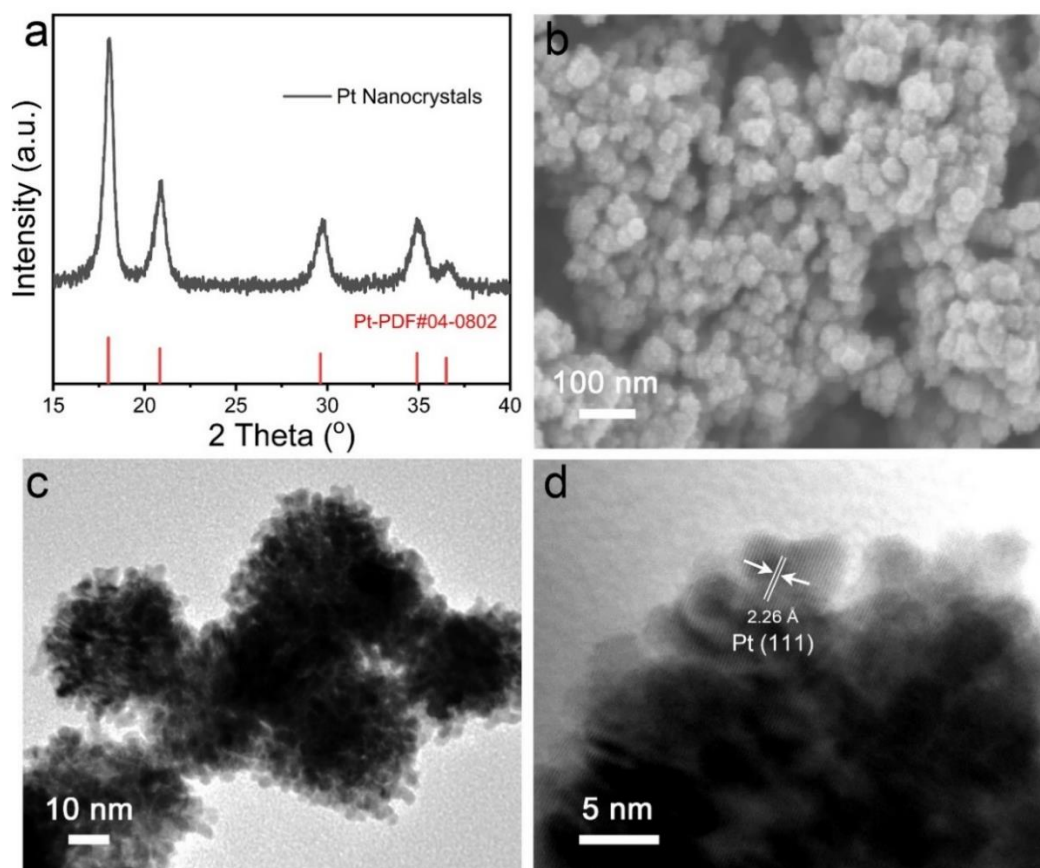
Figure 1. Structure and morphology characterization of blackberry-shaped Pt nanocrystals. (a) XRD pattern, (b) SEM, (c) TEM and (d) HRTEM images of Pt nanocrystals.

shown in **Figure S2**. Then, L-ascorbic acid was chosen as the mild reduction solvent, the temperature chosen of 50 °C ensures a suitable reduction process and spontaneous anisotropic growth occurs, leading to the formation of small and blackberry-shaped nanocrystals, as shown in **Figure S2**. Moreover, the local pH environment is also significant for the reduction process, and Pt^{4+} ions are easily to form clusters in acidic solution.[20] Therefore, boric acid was used to adjust the pH. Adding boric acid has a critical influence on the reduction process of the Pt nanocrystals, as illustrated in **Figure S3**. At first, when the synthetic process was undertaken at 50 °C without adding boric acid, Pt nanocrystals were large and irregular, as shown in **Figure S3a**, the pH was 6.1

before adding reduction solvent. Then the pH was tuned during the synthetic process. The SEM images show corresponding Pt nanocrystals under different pH values of 5.6, 5.2 and 4.9 before adding the reduction solvent. When the pH value was at 5.6, the nanocrystals were smaller but there were still some large particles as shown in **Figure S3b**. Finally, Pt nanocrystals show good shapes and uniformity when the pH was around 5, indicating the suitable pH value. Therefore, ammonium citrate dibasic was used as the surfactant, L-ascorbic acid as the reduction solvent and controlled the reaction in the acid media to successfully synthesize blackberry-shaped Pt nanocrystals at 50 $^{\circ}$C. A reaction mechanism based on slow, continuous nucleation and fast autocatalytic growth can explain the formation of specific Pt nanocrystals in this work.[21] At first, Pt^{4+} ions are slowly reduced by ascorbic acid to form the Pt nanoclusters as the growth seeds. Once the Pt nanoclusters reach a certain size, they become autocatalytic for subsequent Pt reduction. The process is facilitated to a highly anisotropic mode to form single crystals of Pt dendritic feeders on the surface, that finally grow into the mature blackberry-like Pt nanostructure. During the process, the reduction solvent, surfactant, pH environment and temperature all have a synergetic influence on the final size and structure of the Pt nanocrystals. Our work established a simple procedure to fabricate small blackberry-shaped Pt nanocrystals at comparatively low temperature.

2.2 Self-standing Pt nanocrystals on metal foams

The working electrode preparation is always an essential step for an electrocatalysts. Binder solvent, like Nafion, is normally used to fabricate electrocatalysts on current collectors, leading to the decrease of electronic conductivity and a complicated

fabrication process. The dissolution and dispersion of electrocatalysts are inevitable steps during the electrode preparation, having a direct influence on the sufficient numbers of active sites between the nanocrystals and substrates. The interaction between current collectors and active materials is generally ignored, which is even more important for gas release under high current densities. Therefore, self-standing electrocatalysts with robust physical interactions between electrocatalysts and current collectors are promising candidates. Here, different metal substrates are selected to study suitable current collectors for the direct growth of Pt nanocrystals. The Gibbs free energy of hydrogen adsorption ($\triangle G_{*H}$) is one of the significant parameters of HER activity. Copper, nickel and titanium foams are very common substrates, and the top view of Ti(111), Ni(111) and Cu(111) slabs adsorbed with Pt clusters, *i.e.* Pt@Ti, Pt@Ni and Pt@Cu, are shown in **Figure 2a.** Two elementary electrochemical steps of the HER in neutral conditions (pH = 7.2) and the free energy diagram are shown in **Figure 2b.** At 0 V *vs.* SHE, the rate-limiting step for all three catalysts is the water dissociation step and the corresponding limiting potentials are -0.600 eV (Pt@Ti), -0.744 eV (Pt@Ni) and -0.513 eV (Pt@Cu), respectively. Therefore, Pt@Cu is the most efficient HER catalyst among the three electrodes investigated. The equilibrium potential in neutral media is 0.426 V and the free energy under this potential is presented in **Figure 2c**. The adsorption energy of *H, ΔG_{*H}, for Pt@Ti, Pt@Ni and Pt@Cu are -0.174, -0.318 and -0.087 eV, respectively. Combining with the values in **Figure 2c**, it is clear that ΔG_{*H} is a reasonable descriptor of hydrogen evolution activity on HER catalysts.

The ideal HER catalyst should have a moderate ΔG_{*H}, which is close to 0 eV. The
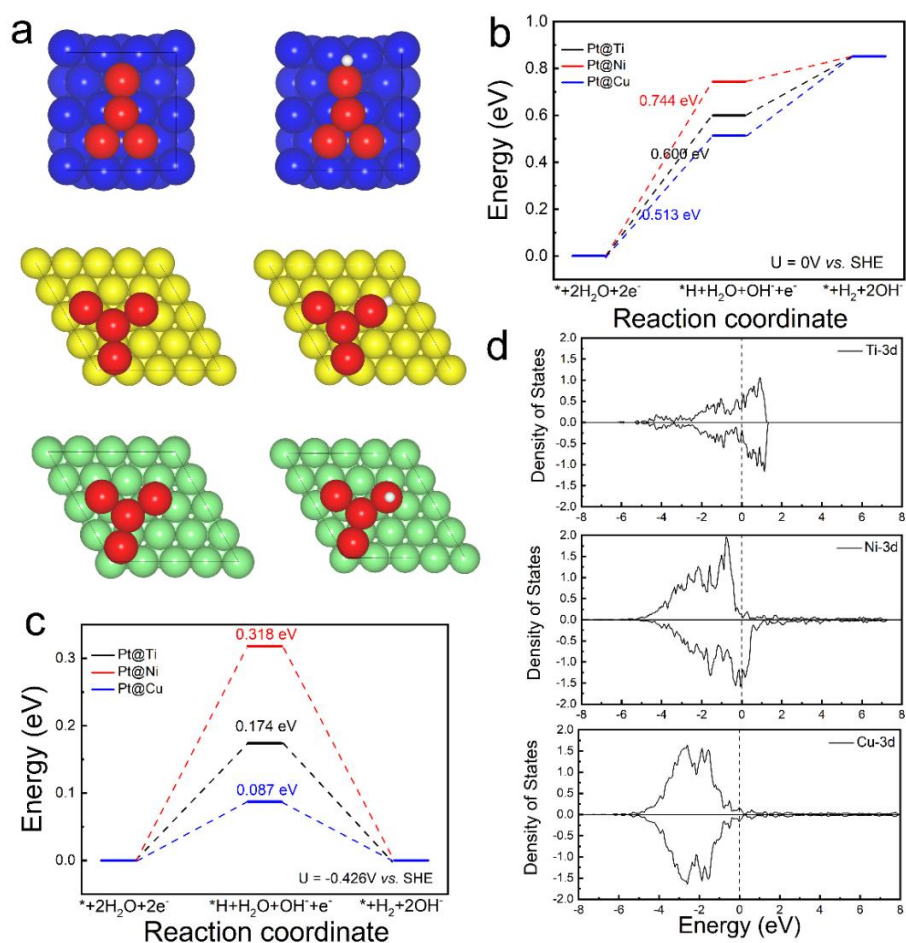
Figure 2. DFT calculation. (a) Top view of Pt@Ti, Pt@Ni and Pt@Cu slabs and the adsorption of H (blue ball, Ti; yellow ball, Ni; green ball, Cu; red ball, Pt; white ball, H). (b) Free energy diagrams of HER on Pt@Ti, Pt@Ni and Pt@Cu at 0 V *vs.* SHE. (c) Free energy diagrams of HER on Pt@Ti, Pt@Ni and Pt@Cu at -0.426 V *vs.* SHE. (d) PDOS 3d states of Ti, Ni and Cu substrates. The Fermi level was taken to be 0 eV.

binding strength between H and Pt@Ti or Pt@Ni is too strong. As shown in **Figure 2a**, with the same initial adsorption positions that *H on the top of the edge Pt atom, the H on Pt@Ti and Pt@Ni can move to the bridge site of Pt and Ti or Pt and Ni while still stay on top of Pt for Pt@Cu. This difference originates from their distinct abilities to adsorb H. The partial density of states (PDOS) of the neighboring substrate atom of the edge Pt is illustrated in **Figure 2d**. Ti and Ni have more charge states near the Fermi level than Cu, which makes them adsorb H more tightly than Cu, thus being responsible

for their less efficient performances in HER catalytic activity. Therefore, the optimization of Pt@Cu electrodes was conducted afterwards by adjusting the Pt loading. The schematic illustration for the fabrication of Pt nanocrystals on Cu foams is shown in **Figure 3a.** The growth of Pt nanocrystals on other foams are under the same conditions. Pt nanocrystals grow directly on Cu foams with a simple reduction method under 50 °C with the assistance of L-ascorbic acid. The original Cu foams have a porous structure and smooth surface, as illustrated in **Figure S4,** providing an ideal surface for the growth of Pt nanocrystals. The as-prepared self-standing electrodes are named as Pt@Cu foams, the labels behind Pt@Cu represent the Pt loading weight per square centimeter (mg cm^{-2}). SEM images in **Figure 3b and 3c** show the morphology of Pt@Cu-0.3, confirming the porous structure and uniform dispersion of Pt nanocrystals on the Cu foam as well as the energy-dispersive X-ray spectroscopy (EDS) mapping images. **Figure S5** exhibits the cross-sectional SEM image, indicating the uniform dispersion of Pt nanocrystals within the porous structure.

Different loading amounts of Pt nanocrystals on Cu foams show distinctive surface morphologies, as shown in **Figure S6**. The Pt loading over 0.6 mg cm^{-2} shows an obvious trend of particle agglomeration, which may lead to the overlap of active sites for HER. Stirring during the synthetic process also has a significant effect, as shown in **Figure S7**. SEM images of Pt@Cu foams with and without stirring during the reduction process show major differences. The large particles are observed on Pt@Cu foams without stirring. Pt nanocrystals remain the blackberry-like shape on Cu foams as shown in the TEM image in **Figure S8**, ensuring more active sites with high roughness.
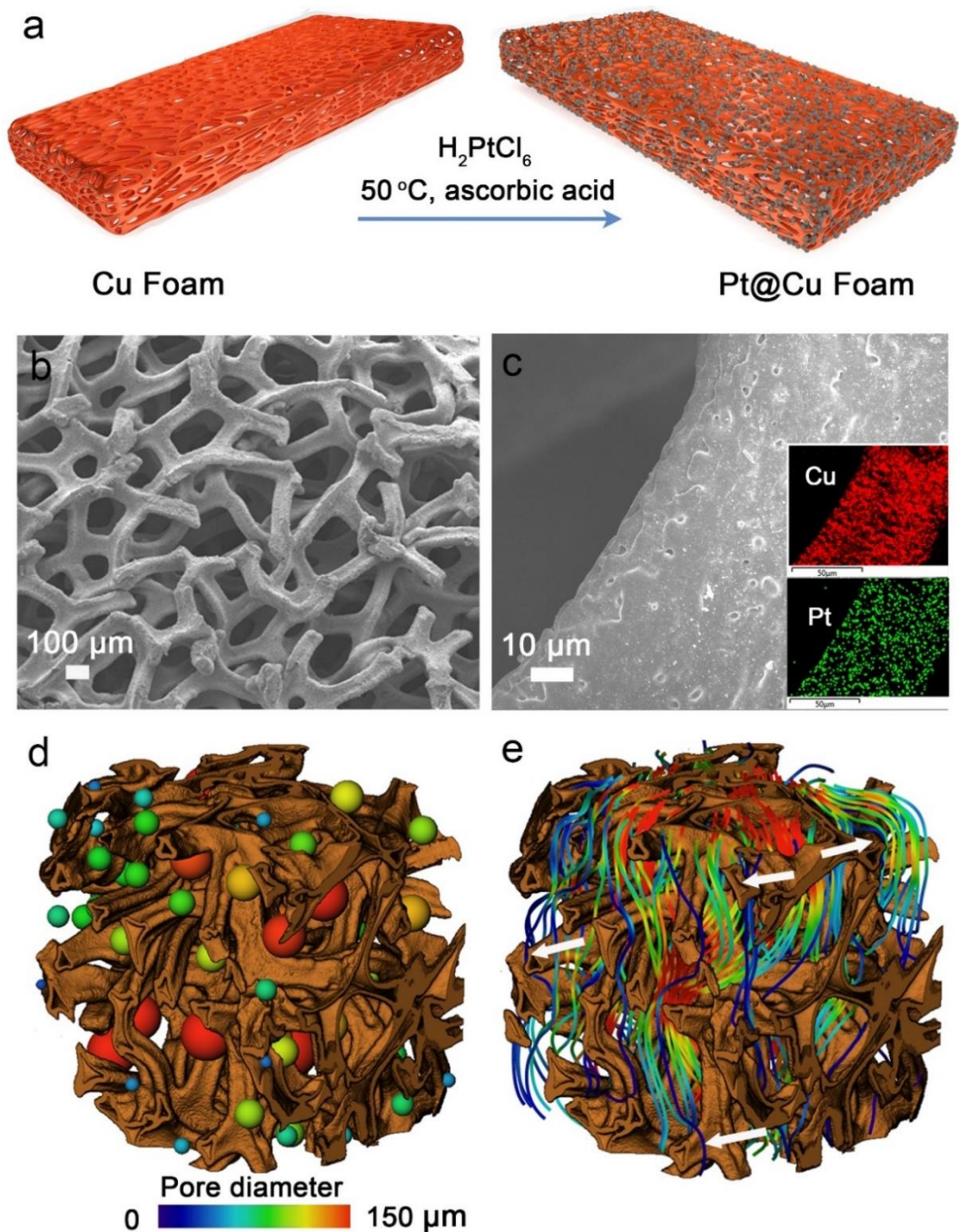
Figure 3. Fabrication schematic and morphology characterization of Pt@Cu. (a) Schematic illustration of the fabrication process for Pt nanocrystals on Cu foams. (b-c) SEM image of Pt@Cu-0.3, insert shows the EDS mapping images. (d). 3D visualization of the Pt@Cu-0.3 foam, with the spheres representing the local pore size reconstructed *via* X-ray computed tomography. (e) Color-coded velocity streamlines of gas flow simulation. The white arrows indicate the locally reduced gas velocity at the foam surface.

The 3D structure of the as-prepared Pt@Cu foam, reconstructed *via* X-ray computed tomography, is visualized in **Figure 3d**, with the spheres of different diameters representing the sizes of the interstitial pores. The porosity is measured to be 0.75 with a tortuosity of 1.4, which ensures good mass transport properties and the fast removal of gas bubbles. **Figure 3e** shows the streamlines of the gas in the permeability simulation, with the colormap showing the relative velocity of the gas flow. It is observed that the gas slows down at the surface of the foam (indicated by the white arrows); however, this is insignificant in determining overall mass transport properties due to the high porosity of the as-prepared foam. The permeability for gas flow was calculated to be 1.08×10^{-12} m^2, which is comparable to the permeability of gas diffusion layers (GDLs) used in proton exchange membrane fuel cells.[22]

2.3 Electrocatalytic activity and durability for HER

Pt@Cu foam shows remarkable performance for HER in 1M phosphate-buffered solution (PBS) with a much lower Pt loading amount compared with commercial Pt/C materials. Commercial Cu foam shows almost no performance during the low potential range, as shown in **Figure 4a**. 0.1 mg cm^{-2} of Pt loading on Cu foam has a small influence on the HER. At a geometric current density of -10 mA cm^{-2}, the overpotentials (η_{10}) of Pt/C@Cu-1 (commercial Pt/C with Nafion solution as the binder), Pt@Cu-0.3, Pt@Cu-0.6 and Pt@Cu-1 are 74 mV, 35 mV, 28 mV and 36 mV, respectively, as shown in **Figure 4a**. With increasing amounts of Pt nanocrystals on the Cu foam, the performance initially rises, but then decreases because of the agglomeration of Pt nanocrystals and a reduced number of efficient active sites. According to the

performance for HER and mass activity curve of Pt loadings in **Figure S9**, Pt@Cu-0.3

shows the best performance. To better understand the remarkable performance of

Pt@Cu foams with different Pt loadings, electrochemically active surface area (ECSA)

was investigated using cyclic voltammetry (CV), as shown in **Figure S10**. The double-

layer capacitances (C_{dl}) of Pt/C@Cu-1, Pt@Cu-0.1, Pt@Cu-0.3, Pt@Cu-0.6 and

Pt@Cu-1 are 12.64 mF cm^{-2}, 2.88 mF cm^{-2}, 37.13 mF cm^{-2}, 46.31 mF cm^{-2} and 42.64

mF cm^{-2}, respectively. The superior performance of Pt@Cu-0.3 foam is due to the high

density of efficient active sites. Increasing the loading amount of Pt nanocrystals tends
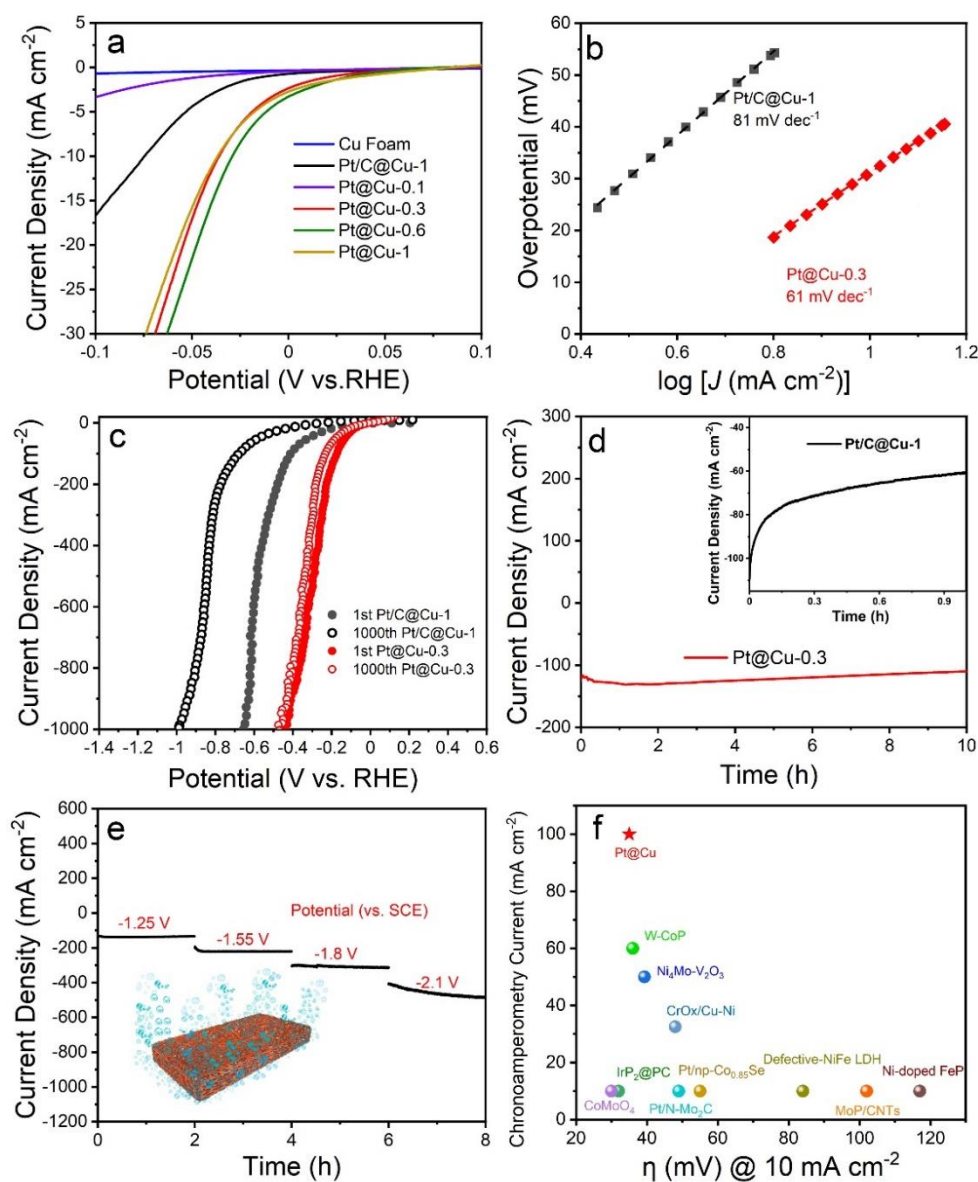
Figure 4. HER performance in 1M PBS. (a) HER performance of Cu foams with different Pt loading amounts and commercial Pt/C in 1M PBS. (b) Tafel plots and (c) 1000 cycles of LSV tests under a scan rate of 100 mV s^{-1} with iR correction of Pt/C@Cu-1 and Pt@Cu-0.3. (d) Chronoamperometry measurement over -100 mA cm^{-2} of Pt@Cu-0.3 in 1M PBS, insert shows the corresponding durability of commercial Pt/C@Cu-1. (e) Chronoamperometry measurements at different high current densities (insert shows H$_2$ bubbles release model). (f) Comparison with the benchmark electrocatalysts by both long-term chronoamperometry current and overpotential to reach -10 mA cm^{-2}, references all performed in neutral medium. Detailed data are listed in **Supplementary Table 1**.

to encourage agglomeration to form large particles, leading to decreased double-layer capacitance. The Pt@Cu-0.3 realizes the most effective performance. The kinetic information is illustrated by the corresponding Tafel plots in **Figure 4b**. The Pt/C@Cu-1 exhibits a Tafel slope of 81 mV dec^{-1}, suggesting both the Heyrovsky and the Volmer reactions are the rate-determining step.[23] The Tafel slope of Pt@Cu-0.3 is 61 mV dec^{-1}, showing the same rate-determining step. Moreover, the synthesized Pt nanocrystals (1 mg cm^{-2}) were pasted on the Cu foam with Nafion solution as binder. The morphology was compared with Pt/C pasted on the Cu foam and self-standing Pt@Cu-0.3, as shown in **Figure S11**. The Pt@Cu-0.3 shows the uniform dispersion of Pt nanocrystals on the Cu foam while Pt nanocrystals and Pt/C pasted on Cu foam show the part aggregation because of the dissolution problem using Nafion binder solution during the preparation process. The size of Pt nanoparticles in Pt/C was around 25 nm from SEM images. The as-prepared electrode was applied for HER in neutral media to make a comparison with Pt/C@Cu-1 and Pt@Cu-0.3, as shown in **Figure S12**. The overpotential Pt NCs@Cu-1 was 68 mV at a current density of -10 mA cm^{-2}, which was

relatively lower than that of commercial Pt/C pasted on Cu foam, but much higher compared to the self-standing Pt@Cu-0.3. The huge HER performance difference was the interaction between Pt and Cu, the Pt@Cu interaction tunes the adsorption hydrogen energy. The Nafion binder only links the Pt with Cu foam and the physical interaction was weak especially under high current densities with fierce bubble release, further confirming the advantage of the self-standing Pt@Cu electrodes.

To further explore the HER performance under high current densities, LSV curves of Pt/C@Cu-1 and Pt@Cu-0.3 were measured under 100 mV s^{-1}, reaching -1000 mA cm^{-2}. The corresponding 1000 cycles of LSV tests were also performed to confirm the robust HER electrodes under the high current density. Under a high current density, the LSV curves with iR correction were shown in **Figure 4c**. Pt@Cu-0.3 shows much faster HER under high current densities compared with Pt/C@Cu-1. The overpotentials at the current density of -1000 mA cm^{-2} for Pt@Cu-0.3 and Pt/C@Cu-1 were 438 mV and 654 mV. After 1000 cycles of LSV tests, the overpotentials increased to 470 mV and 985 mV, respectively. The small overpotential change of Pt@Cu-0.3 electrode under 1000 cycles of LSV tests confirmed the stability and robust interaction between Pt and Cu. While the huge overpotential change of Pt/C@Cu-1 was ascribed to the weak interaction under fierce bubble release. LSV curves without iR correction are listed in **Figure S13**.

The results of electrochemical impedance spectroscopy (EIS) are illustrated in **Figure S14**, CPE$_a$ and CPE$_b$ represent the constant phase element and resistance related to the surface porosity; R_s indicates the series resistance; R_p and R_{ct} represent the polarization

resistance and charge transfer resistance of the HER process. The R_{ct} of Pt/C@Cu-1 and Pt@Cu-0.3 are 284.7 and 3.79 Ω by fitting the model of Nyquist plots, respectively. The superior performance of Pt@Cu-0.3 is determined from the small R_{ct} through the measurements, suggesting the high conductivity and improved charge transfer capability.[24] A chronoamperometry test of as-prepared electrodes was performed to study the stability of electrocatalysts. Under a constant potential, the durability is related to both the physical and chemical stability of materials, especially under high current densities for HER. As shown in **Figure 4d**, under a constant potential of -1.25 V (*vs*. SCE), the current density of Pt@Cu-0.3 is over -100 mA cm^{-2} for 10 h, decreases from -117 mA cm^{-2} to -110 mA cm^{-2}, which represents extraordinary stability for Pt-based electrocatalysts in 1 M PBS. The corresponding overpotentials increased from 168 mV to 195 mV with iR compensation. By comparison, the Pt/C@Cu-1 shows poor durability after only one hour, mostly because of the weak binding between Pt/C and the substrate under the physically aggregation caused by H_2 bubbles production on the electrodes, as inserted in **Figure 4d**. This problem is normal for working electrodes prepared with binder solvents, especially under high current densities. The strong interaction between the Pt and Cu foam is also reflected by the strong ultrasonication of Pt@Cu foam in aqueous media for 1 hour, during which there was no observed precipitation in **Figure S15**. Moreover, the self-standing Pt nanocrystals on Cu foam shows excellent durability in neutral media, even under higher current densities. The applied constant potential was increased every two hours to boost the reaction rate, as shown in **Figure 4e**. The durability is remarkable when the current densities are at level

of -100 mA cm^{-2}, -200 mA cm^{-2}, -300 mA cm^{-2} and -400 mA cm^{-2}, the applied constant

voltages are -1.25 V, -1.55 V, -1.8 V and -2.1 V (*vs*. SCE), respectively. The robust self-

standing Pt nanocrystals and porous structures ensure stability with rapid hydrogen

release, as shown insert in the model picture, which is consistent with the tomography

analysis. The comparison with reported benchmark catalysts, as for both the long-term

chronoamperometry current and the overpotential to reach the current density of -10

mA cm^{-2} in 1 M PBS, is shown in **Figure 4f**. Pt@Cu-0.3 shows the best-in-class

performance and robust stability (detailed data in **Supplementary Table 1**). The

overpotentials of reported work are all calculated with 100% iR compensation, at a

certain current density of -10 mA cm^{-2}, its iR compensation was related to the internal

resistance directly, which was plotted from Nyquist curves of electrochemical

impedance spectra. In **Figure S16**, the internal resistances of commercial Pt/C@Cu-1

and Pt@Cu-0.3 were 3.06 Ω and 2.84 Ω. The LSV curves and related iR corrected

curves of Pt@Cu-0.3 and Pt/C@Cu-1 were shown. More importantly, the synthetic

method is more facile and at low temperature without the need for a protective

atmosphere. The Pt@Cu-0.3 electrode was also applied for HER in both acidic and

alkaline media, as shown in **Figure S17**. The overpotentials of Pt@Cu-0.3 at a current

density of -10 mA cm^{-2} in acidic and alkaline electrolytes were 67 mV and 33 mV,

indicating its outstanding performance for HER over a wide pH range. To present the

extensive utilization of the uniform Pt nanostructure synthetic strategy in this work, Ni

and Ti foams were also used as metal substrates to directly grow Pt nanocrystals. The

morphology and HER performance were characterized. **Figure S18** shows the SEM

images of morphology for Pt@Ni and Pt@Ti. The HER performance of Pt nanocrystals formed on different foams was compared, as shown in **Figure S19**. At a current density of -10 mA cm^{-2}, the average overpotentials of Pt@Ni-0.3, Pt@Ti-0.3 and Pt@Cu-0.3 with multiple HER tests were 41.1 mV, 43.8 mV and 35.1 mV, respectively, indicating the intuitive overpotential difference of Pt on Cu, Ni and Ti foams.Therefore, Pt nanocrystals loaded on Cu foam has the best performance, which is consistent with the DFT predictions. The durability under constant voltage of Pt@Ti-0.3 and Pt@Ni-0.3 in 1M PBS over -100 mA cm^{-2} is shown in **Figure S20**. The durability for Pt@Ni is much better than Pt@Ti, but not as good as Pt@Cu. In summary, different metal substrates have significant influences on the HER performance and durability with the *in-situ* growth of Pt nanocrystals, and Cu foam is the most suitable choice among these three substrates. This binder-free Pt-based electrocatalysts design provides a new strategy to combine suitable current collectors and electrocatalysts for efficient electrocatalytic processes, especially under high current densities.

2.4 XPS analysis of as-prepared electrodes

The remarkable durability at high current densities is attributed to the robust interaction between Pt and Cu foams and porous structures, the efficient performance of Pt@Cu foam is due to tuning of the appropriate hydrogen free energy by the combination of Pt and Cu. The change of surface chemical environment before and after reaction is further studied by X-ray photoelectron spectroscopy (XPS), as shown in **Figure 5**. In previous work, many experimental and theoretical attempts pointed out that key steps in neutral media begin with the water dissociation, ($H_2O + e^- + M \rightarrow M-^*H + OH^-$, where M

stands for the metal and *H is the adsorbed H)[4], Pt has the most ideal hydrogen adsorption free energy, and are followed by either the electrochemical Heyrovsky step ($H_2O + M-*H + e^- \rightarrow M + H_2 + OH^-$) or the chemical Tafel recombination step ($2*H \rightarrow H_2$), Pt shows the most suitable adsorption energy of H, but in neural media, the Pt material itself exhibits limited performance compared with that in acidic media. Here, Cu foams are introduced as the substrate, the Cu surface after Pt loading has an important effect for HER, as confirmed by DFT calculation, which is much more efficient for water dissociation.

The XRD patterns in **Figure 5a** show almost no difference before and after the durability test of the Pt@Cu foam in 1M PBS. However, the XPS spectra provide more detailed information, which helps to understand the surface chemical environment changes of Pt and Cu. In the deconvoluted Cu 2p XPS spectra, peaks located at 932.6 and 952.4 eV represent the Cu $2p_{3/2}$ and Cu $2p_{1/2}$ of elemental Cu, respectively.[25] Moreover, the obvious peak at 934.6 eV indicates the existence of $Cu(OH)_2$, which was confirmed by previous work.[26] The formation of a small amount of $Cu(OH)_2$ was inevitable during the synthesis process. It was proved that metal hydroxide (M–OH) promotes water dissociation, providing a proton at the metal/hydroxide interface which then combines with a second proton to generate H_2 on the metal surface.[16] To further confirm the positive effect between Pt and $Cu(OH)_2$, we chose carbon paper as the substrate and used Nafion solution as the binder to paste Pt nanocrystals and $Pt/Cu(OH)_2$ mixture on substrates. The as-prepared electrodes were applied for HER in 1M PBS. The loadings of Pt nanocrystals were both 1 mg cm^{-2}. The extra adding of

Cu(OH)$_2$ was 0.5 mg cm^{-2}. As shown in **Figure S21**, LSV curves were very similar but there was still a small difference. The overpotentials at a current density of -10 mA cm^{-2} of Pt@Carbon Paper and Pt/Cu(OH)$_2$@Carbon Paper were 72.3 mV and 67.5 mV. The small difference indicated the positive effect of Cu(OH)$_2$ on the enhancement of electrocatalytic activity in neutral media, but the main effect was the interaction between Pt and Cu.
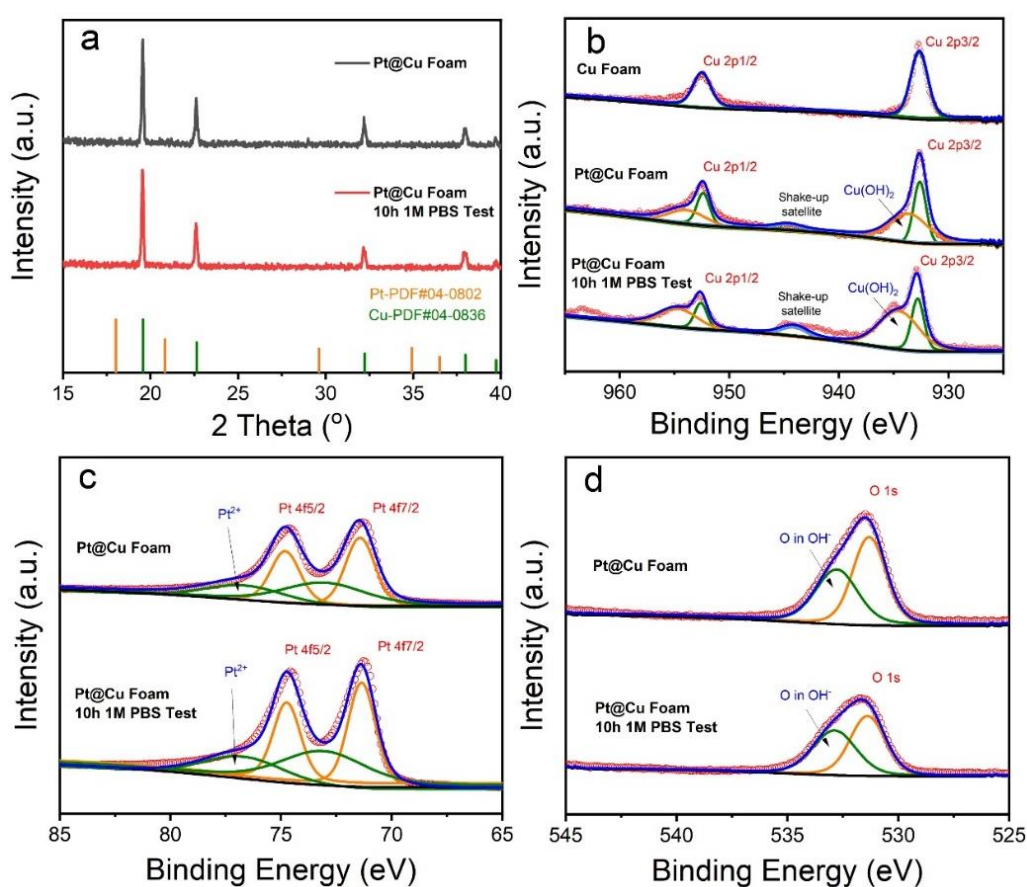
Figure 5. XRD and XPS characterizations of Pt@Cu foam before and after the durability test. (a) XRD patterns of Pt@Cu foam before and after the durability test in 1M PBS at -100 mA cm^{-2}. XPS spectra of (b) Cu 2p, (c) Pt 4f and (d) O 1s of Pt@Cu foam before and after the durability test in 1 M PBS at -100 mA cm^{-2}.

After the chronoamperometry test, the shake-up satellite peak increases, which is normal for the copper substrate, indicating the increased formation of Cu(OH)$_2$, having

a positive influence on HER. XPS spectra shown in **Figure 5c** indicate the chemical composition and binding states of the Pt nanocrystals. The paired peaks at 71.4 and 74.7 eV are ascribed to metallic Pt^0.[27] The other paired peaks located at 73.1 and 76.7 eV represent the Pt^{2+} species.[28] Pt^{2+} may be ascribed to oxidation when exposed to air and Pt^0 is the dominant chemical state on the copper surface. Both Pt and Pt^{2+} peaks have almost no changes after the chronoamperometry test, indicating its stable chemical environment on Cu foams. The deconvolution of the O peak at 532.8 eV in **Figure 5d** is attributed to the OH^- group on the metal hydroxides.[25] The ratio of OH^- signals in the O peak increases moderately after the chronoamperometry test, which corresponds to the increased amount of $Cu(OH)_2$ on the Cu surface. The chemical environment signals of Pt@Cu further confirmed the stable chemical environment of Pt nanocrystals, and the existence of $Cu(OH)_2$ on the surface, which suggests the design of hybrid electrocatalysts for HER in neutral media.
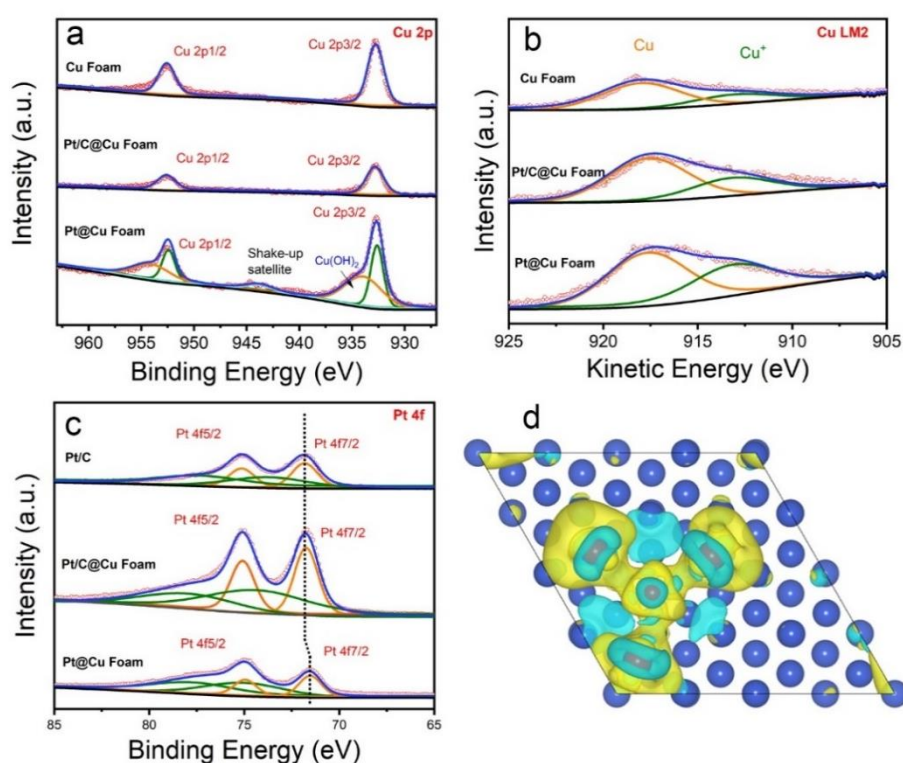
Figure 6. XPS characterization and charge density difference between Pt and Cu. XPS spectra of (a) Cu 2p, (b) Cu LM2 and (c) Pt 4f of Cu foam, Pt/C powder, Pt/C@Cu foam and Pt@Cu foam. (d) Charge density difference of Pt@Cu. Charge accumulation and depletion are presented by yellow and cyan isosurfaces and isosurface levels are set as 0.005 Bohr^{-3} (blue ball, Cu; red ball, Pt).

To explore the interaction between Pt and Cu, we further acquired the XPS data and simulation work of the charge density difference between Pt and Cu, as shown in **Figure 6**. The **Figure 6a** illustrated the XPS spectra of Cu 2p of Cu foam, Pt/C pasted on Cu foam and self-standing Pt@Cu foam. As described previously, Cu(OH)$_2$ appeared during *in-situ* growth process. Pt/C pasted foams had the same peaks as the Cu foam in XPS spectra of Cu 2p. Then Auger kinetic energy peaks were fitted into two peaks, representing Cu$^+$ and Cu^0, as shown in **Figure 6b**. The surface ratios of Cu$^+$/Cu^0 for Cu foam, Pt/C@Cu and Pt@Cu were 0.34, 0.38 and 0.54, respectively, indicating the obvious chemical environment changes of Pt@Cu. The dramatically increased Cu$^+$ shows more electrons transfer between Cu and Pt.[29] The core level XPS spectra of Pt 4f of Pt/C powder, Pt/C pasted on Cu foam and Pt@Cu foam were listed in **Figure 6c**. The peak of Pt/C located at 71.8 eV was ascribed to Pt^0. The corresponding peaks of Pt/C@Cu and Pt@Cu were 71.8 and 71.4 eV. The shift binding energy of Pt@Cu was 0.4 eV, indicating an increase in the electron density around Pt^0 compared with that of Pt/C@Cu.[30] The charge density difference between Pt and Cu was calculated, as shown in **Figure 6d**. The charge accumulation and depletion were presented by yellow and cyan isosurfaces, suggesting obvious charge exchange between Cu and Pt atoms, which ensures strong interactions between Cu and Pt. The experimental and theoretical

results both confirmed the increased electrons transfer and strong interaction between Pt and Cu for self-standing Pt@Cu electrode.

3. Conclusion

In summary, we present a facile method of *in-situ* growth of Pt nanocrystals with high roughness on Cu foams. This material shows high efficiency and durability for HER in neutral media. The strong interaction between Cu and Pt, illustrated by charge density difference and XPS analysis, ensures high durability as self-standing electrodes in neutral media and the porous structure is efficient for the rapid release of generated H_2, consistent with X-ray tomography analysis. DFT calculation reveals tuning of the hydrogen free energy on the Pt@Cu interface close to zero can realize the efficient proton adsorption energy and the fast release of generated molecular hydrogen. Moreover, the XPS analysis indicates the stable surface chemical environment and the existence of copper hydroxide on the surface, which has positive effects for the water dissociation process in neutral media. The self-standing Pt@Cu exhibits advantages of low overpotentials of 35 and 438 mV to reach current densities of -10 and -1000 mA cm^{-2} respectively and outstanding durability, even at -400 mA cm^{-2}. The excellent stability reflected by 1000 cycles of LSV tests reaching -1000 mA cm^{-2} further confirm the strong interaction between Pt and Cu. Our findings study the interaction between suitable current collectors and electrocatalytic materials and provide a simple way to fabricate self-standing electrodes under mild conditions that lower the amount and hence cost of materials required for HER in neutral media, ensuring stable HER performance, especially under high current densities.

4. Experimental Section

4.1 Materials

Chloroplatinic acid hexahydrate ($H_2PtCl_6 \cdot H_2O$, 8 wt%Pt) was purchased from Sigma-Aldrich (UK) Co., Ltd. Ammonium citrate dibasic ($HOC(CO_2H)(CH_2CO_2NH_4)_2$) was purchased from Sigma-Aldrich (UK) Co., Ltd. L-Ascorbic acid ($C_6H_8O_6$) was purchased from Merck (USA) Co., Ltd. Boric acid (H_3BO_3) was purchased from Alfa Aesar (UK) Co., Ltd. Potassium dihydrogen phosphate (KH_2PO_4) and potassium phosphate dibasic (K_2HPO_4) were purchased from Alfa Aesar (UK) Co., Ltd. Copper hydroxide $Cu(OH)_2$ was purchased from Sigam-Aldrich (UK) Co., Ltd. Polyvinylpyrrolidone (PVP) was purchased from Sigam-Aldrich (UK) Co., Ltd. Nafion solution was purchased from Sigam-Aldrich (UK) Co., Ltd. All chemicals were used as received without further purification.

4.2 Preparation of Pt nanocrystals and Pt@Cu foam with different Pt loadings.

In a typical fabrication process, both 0.905 g of ammonium citrate dibasic and 0.705 g of L-ascorbic acid were dissolved in 40 mL of deionized (DI) water. Then 0.185 g of boric acid was dissolved in 30 mL of DI water. Commercial Cu foams (2 cm×1 cm) were used as the substrates for free-standing electrodes. To remove possible surface oxide layers, Cu foams were immersed into 0.5 M hydrochloric acid solution for ~ 5 min under ultrasonication. Afterwards, Cu foams were washed by DI water and dried in a vacuum oven at 70 °C for 2 hours. Then, Cu foams were put in a 100 mL beaker under magnetic stirring with 10 mL DI water. 10 mL of the as-prepared 0.1 M ammonium citrate dibasic solution was mixed with 50, 75, 100, 125 μL of

chloroplatinic acid hexahydrate solution for different Pt loading amounts in the beaker. The boric acid was added to the beaker to adjust the pH value and the solution was stirred for 20 mins at room temperature. Finally, the solution was heated up to 50 $^{\circ}$C. After the temperature reached 50 $^{\circ}$C, 10 mL of 0.1 M L-ascorbic acid solution was added immediately. The first solution was transparent, then became dark gray and Cu foams slowly became grey due to the *in-situ* growth of Pt nanocrystals; the whole process lasted for 1 hour. The Pt nanocrystals were fabricated with the same process except adding Cu foam. Different metal foams were also subjected to the same method. After the reaction, Pt@Cu foams with different Pt loadings had been successfully fabricated and were washed by DI water and dried in an oven overnight at 70 $^{\circ}$C. Different Pt loading with different amounts of H_2PtCl_6 are listed in **Figure S22**.

4.3 Preparation of working electrode with Nafion binder

In a typical fabrication process, 1 mg as-prepared Pt nanocrystals or 5 mg commercial 20% Pt/C powder was dispersed in solution with 200 µl DI water, 50 µl ethonal and 10 µl Nafion solution, then droped on 1 cm^{-2} of Cu foam to fabricate the Pt NCs@Cu-1 and Pt/C@Cu-1 electrodes. Extra $Cu(OH)_2$ was prepared through the same process.

4.4 Characterization

X-ray diffraction (XRD) patterns were obtained using a STOE SEIFERT diffractometer with a detected angular range of 2° < 2θ < 40° with a Mo X-ray radiation source. The surface morphology and chemical dispersion of the as-prepared foams and nanocrystals were characterized by scanning electron microscopy (SEM, Carl Zeiss EVO MA10) and transmission electron microscopy (TEM JEOL and JEM-2100). The chemical

states of different elements were evaluated by X-ray photoelectron spectroscopy (XPS, Thermo Scientific K-alpha photoelectron spectrometer) analysis. Date analysis of XPS results was achieved using CasaXPS with the calibration of C 1s 284.8 eV. The 3D microstructure of the as-prepared foam was obtained using a lab-based X-ray computed tomography microscope (Zeiss Xradia Versa 520). A total number of 2001 projections were sequentially acquired at the voxel size of 0.77 mm and an exposure time of 3 seconds/frame while the sample is being rotated over 360°. Built-in Feldkamp-Davis-Kress (FDK) algorithm was used for the reconstruction.[31] The 3D visualization and pore size quantification were achieved using the commercial software Avizo V9.5 (ThermoFisher Scientific). The permeability simulation was conducted using Avizo XLabSuite Extension package by solving the Navier-Stokes equation with a pressure drop as the boundary condition. The pH value was acquired by HI2550 Meter.

4.5 Electrochemical measurements

In a typical electrochemical experiment, measurements of as-prepared self-standing electrodes were conducted in a three-electrode cell. 1M PBS solution was used as the electrolyte mixed with volume ratio of 1 : 1 between K_2HPO_4 and KH_2PO_4. 1M KOH and 0.5M H_2SO_4 were also used as electrolyte. The counter electrode was a graphite rod. Additionally, an Ag/AgCl electrode (filled with 3M KCl) was used as a reference electrode. The as-prepared Cu/Pt foams were used as the working electrode. 1 cm^{-2} of the metal foam was controlled to immerse in the electrolyte during the test. Cyclic voltammetry (CV) and linear sweep voltammetry (LSV) measurements were carried out using a Gamry Interface 1000 potentiostat. All the potentials were converted to the

reversible hydrogen electrode (RHE) according to the equation $E_{RHE} = E_{Ag/AgCl}+0.197+0.059pH$. Tafel slopes were determined by fitting the linear regions of the Tafel plots according to the Tafel equation (η = b log(j) + a) and replotted polarization curves. The high current density stability was evaluated by the chronoamperometry measurement. Electrochemical impedance spectroscopy (EIS) was performed with frequencies from 0.1 to 100,000 Hz with an amplitude of 10 mV. All the LSV measurements were calculated with 100% iR compensation except special statement. The LSV curves reaching 1000 mA cm^{-2} were reported with 90% iR compensation.[32]

4.6 Computational simulation

All the density functional theory (DFT) calculations were performed *via* the Vienna Ab initio Simulation package (VASP),[33] and the projector-augmented plane wave (PAW) pseudopotentials were used for the elements involved.[34] The generalized gradient approximation (GGA) of Perdew, Burke, and Ernzerhof (PBE) was used to treat the exchange-correlation between electrons.[35] Ti(111), Ni(111) and Cu(111) slabs adsorbed with Pt clusters, Pt@Ti, Pt@Ni and Pt@Cu, are shown in **Figure 2a.** There are four layers in each slab and the bottom two layers keep fixed during the calculation. A vacuum region of greater than 15 Å was added along the direction normal to the slab plane to avoid the interaction between periodic supercells. The electron wave function is expanded in plane waves and a cutoff energy of 550 eV is chosen. The Monkhorst-Pack meshes of (3, 3, 1) were adopted for the Brillouin zone (BZ) of the slabs, while denser k-points of (7, 7, 1) were employed for electronic property computations.[36] The

convergence in the energy and force were set to be 10^{-4} eV and 0.01 eV Å^{-1}, respectively. The free energies of H$_2$O(l) and H$_2$(g) were used as references when calculating the free energies of reaction intermediates. The adsorption energy for reaction intermediate is calculated as follows: [37]

$$\Delta G = \Delta E_{Total} + \Delta E_{ZEP} - T\Delta S + \Delta G_s - 0.0592*pH - eU \ (1)$$

where ΔE_{Total} is the calculated adsorption total energy by DFT, ΔE_{ZPE} is zero-point energy, ΔS is entropy, and ΔG_s is solvation energy. [38] HER in neutral media proceeds first through water dissociation (* + H$_2$O + e$^-$ → *H + OH$^-$), followed by hydrogen formation *via* either Heyrovsky step (*H + H$_2$O + e$^-$ → * + H$_2$ + OH$^-$) or Tafel step (2*H → *+ H$_2$), where * denotes a possible reaction site. The calculated HER electrochemical potential can be obtained as follows:

$$U_L = Mini[-\Delta G_i] \ / \ ne \ (2)$$

where n is the number of electrons transferred for each electrochemical step, and e is the elementary charge. Here, n is set to 1 for the one-electron transfer step. The meaning of the r.h.s. of the above equation is to select the smallest $[-\Delta G_i]$ among the HER elementary steps.

5 Acknowledgments

6 Supporting Information

Additional characterization including SEM, TEM, CV curves and ECSA curves are provided.

7 Conflict of Interest

The authors declare no conflict of interest.

References

[1] a) X. Zou, Y. Zhang, *Chem. Soc. Rev.* **2015**, *44*, 5148-5180; b) D. Voiry, H. Yamaguchi, J. Li, R. Silva, D. C. B. Alves, T. Fujita, M. Chen, T. Asefa, V. B. Shenoy, G. Eda, M. Chhowalla, *Nat. Mater.* **2013**, *12*, 850-855; c) M. Cabán-Acevedo, M. L. Stone, J. R. Schmidt, J. G. Thomas, Q. Ding, H.-C. Chang, M.-L. Tsai, J.-H. He, S. Jin, *Nat. Mater.* **2015**, *14*, 1245-1251; d) X. Wang, L. Chen, S. Y. Chong, M. A. Little, Y. Wu, W.-H. Zhu, R. Clowes, Y. Yan, M. A. Zwijnenburg, R. S. Sprick, A. I. Cooper, *Nat. Chem.* **2018**, *10*, 1180-1189.

[2] a) P. Xiao, M. A. Sk, L. Thia, X. Ge, R. J. Lim, J.-Y. Wang, K. H. Lim, X. Wang, *Energy Environ. Sci.* **2014**, *7*, 2624-2629; b) D. Voiry, M. Salehi, R. Silva, T. Fujita, M. Chen, T. Asefa, V. B. Shenoy, G. Eda, M. Chhowalla, *Nano Lett.* **2013**, *13*, 6222-6227; c) M.-R. Gao, J.-X. Liang, Y.-R. Zheng, Y.-F. Xu, J. Jiang, Q. Gao, J. Li, S.-H. Yu, *Nat. Commun.* **2015**, *6*, 5982; d) L. Zhao, Y. Zhang, Z. Zhao, Q.-H. Zhang, L.-B. Huang, L. Gu, G. Lu, J.-S. Hu, L.-J. Wan, *Natl. Sci. Rev.* **2020**, *7*, 27-36.

[3] D. Liu, X. Li, S. Chen, H. Yan, C. Wang, C. Wu, Y. A. Haleem, S. Duan, J. Lu, B. Ge, P. M. Ajayan, Y. Luo, J. Jiang, L. Song, *Nat. Energy* **2019**, *4*, 512-518.

[4] C.-T. Dinh, A. Jain, F. P. G. de Arquer, P. De Luna, J. Li, N. Wang, X. Zheng, J. Cai, B. Z. Gregory, O. Voznyy, B. Zhang, M. Liu, D. Sinton, E. J. Crumlin, E. H. Sargent, *Nat. Energy* **2019**, *4*, 107-114.

[5] a) Y.-Y. Ma, C.-X. Wu, X.-J. Feng, H.-Q. Tan, L.-K. Yan, Y. Liu, Z.-H. Kang, E.-B. Wang, Y.-G. Li, *Energy Environ. Sci.* **2017**, *10*, 788-798; b) X. Wu, S. Zhou, Z. Wang, J. Liu, W. Pei, P. Yang, J. Zhao, J. Qiu, *Adv. Energy Mater.* **2019**, *9*, 1901333; c) J. Miao, Z. Lang, X. Zhang, W. Kong, O. Peng, Y. Yang, S. Wang, J. Cheng, T. He, A. Amini, Q. Wu, Z. Zheng, Z. Tang, C. Cheng, *Adv. Funct. Mater.* **2019**, *29*, 1805893.

[6] a) X. Zou, X. Huang, A. Goswami, R. Silva, B. R. Sathe, E. Mikmeková, T. Asefa, *Angew. Chem. Int. Ed.* **2014**, *53*, 4372-4376; b) R. Zhang, X. Wang, S. Yu, T. Wen, X. Zhu, F. Yang, X. Sun, X. Wang, W. Hu, *Adv. Mater.* **2017**, *29*, 1605502; c) K. Li, J. Zhang, R. Wu, Y. Yu, B. Zhang, *Adv. Sci.* **2016**, *3*, 1500426.

[7] Y. Liang, Q. Liu, A. M. Asiri, X. Sun, Y. Luo, *ACS Catal.* **2014**, *4*, 4065-4069.

[8] H. Zhang, P. An, W. Zhou, B. Y. Guan, P. Zhang, J. Dong, X. W. Lou, *Sci. Adv.* **2018**, *4*, eaao6657.

[9] J.-X. Feng, H. Xu, S.-H. Ye, G. Ouyang, Y.-X. Tong, G.-R. Li, *Angew. Chem. Int. Ed.* **2017**, *56*, 8120-8124.

[10] a) H. Zhou, F. Yu, Y. Huang, J. Sun, Z. Zhu, R. J. Nielsen, R. He, J. Bao, W. A. Goddard Iii, S. Chen, Z. Ren, *Nat. Commun.* **2016**, *7*, 12765; b) C. Tang, L. Gan, R. Zhang, W. Lu, X. Jiang, A. M. Asiri, X. Sun, J. Wang, L. Chen, *Nano Lett.* **2016**, *16*, 6617-6621; c) H. Zhou, F. Yu, Y. Liu, J. Sun, Z. Zhu, R. He, J. Bao, W. A. Goddard, S. Chen, Z. Ren, *Energy Environ. Sci.* **2017**, *10*, 1487-1492.

[11] P. Nayak, Q. Jiang, N. Kurra, X. Wang, U. Buttner, H. N. Alshareef, *J. Mater. Chem. A* **2017**, *5*, 20422-20427.

[12] Z. Wang, X. Ren, Y. Luo, L. Wang, G. Cui, F. Xie, H. Wang, Y. Xie, X. Sun, *Nanoscale* **2018**, *10*, 12302-12307.

[13] a) L. Xiu, W. Pei, S. Zhou, Z. Wang, P. Yang, J. Zhao, J. Qiu, *Adv. Funct. Mater.* **2020**, *30*, 1910028; b) L. Zhang, L. Han, H. Liu, X. Liu, J. Luo, *Angew. Chem. Int. Ed.* **2017**, *56*, 13694-13698; c) J. Zhang, Y. Zhao, X. Guo, C. Chen, C.-L. Dong, R.-S. Liu, C.-P. Han, Y. Li, Y. Gogotsi, G. Wang, *Nat. Catal.* **2018**, *1*, 985-992.

[14] S. Li, C. Cheng, A. Sagaltchik, P. Pachfule, C. Zhao, A. Thomas, *Adv. Funct. Mater.* **2019**, *29*, 1807419.

[15] G. Qian, J. Chen, T. Yu, L. Luo, S. Yin, *Nano-Micro Lett.* **2021**, *13*, 77.

[16] a) Z. Zhu, H. Yin, C.-T. He, M. Al-Mamun, P. Liu, L. Jiang, Y. Zhao, Y. Wang, H.-G. Yang, Z. Tang, D. Wang, X.-M. Chen, H. Zhao, *Adv. Mater.* **2018**, *30*, 1801171; b) G. Chen, T. Wang, J. Zhang, P. Liu, H. Sun, X. Zhuang, M. Chen, X. Feng, *Adv. Mater.* **2018**, *30*, 1706279.

[17] N. Cheng, S. Stambula, D. Wang, M. N. Banis, J. Liu, A. Riese, B. Xiao, R. Li, T.-K. Sham, L.-M. Liu, G. A. Botton, X. Sun, *Nat. Commun.* **2016**, *7*, 13638.

[18] L. Wang, Y. Yamauchi, *J. Am. Chem. Soc.* **2009**, *131*, 9152-9153.

[19] X. Sun, J. He, Y. Meng, L. Zhang, S. Zhang, X. Ma, S. Dey, J. Zhao, Y. Lei, *J. Mater. Chem. A* **2016**, *4*, 4161-4171.

[20] M. H. Ullah, W.-S. Chung, I. Kim, C.-S. Ha, *Small* **2006**, *2*, 870-873.

[21] a) L. Wang, Y. Yamauchi, *Chem. Mater.* **2009**, *21*, 3562-3569; b) Y. Song, Y. Yang, C. J. Medforth, E. Pereira, A. K. Singh, H. Xu, Y. Jiang, C. J. Brinker, F. van Swol, J. A. Shelnutt, *J. Am. Chem. Soc.* **2004**, *126*, 635-645.

[22] B. K. Kanchan, P. Randive, S. Pati, *Int. J. Hydrogen Energy* **2020**, *45*, 21836-21847.

[23] R. Xu, L. Kang, J. Knossalla, J. Mielby, Q. Wang, B. Wang, J. Feng, G. He, Y. Qin, J. Xie, A.-C. Swertz, Q. He, S. Kegnæs, D. J. L. Brett, F. Schüth, F. R. Wang, *ACS Nano* **2019**, *13*, 2463-2472.

[24] D. Strmcnik, P. P. Lopes, B. Genorio, V. R. Stamenkovic, N. M. Markovic, *Nano Energy* **2016**, *29*, 29-36.

[25] O. Akhavan, R. Azimirad, S. Safa, E. Hasani, *J. Mater. Chem.* **2011**, *21*, 9634-9640.

[26] X. Zhao, M. Deng, G. Rao, Y. Yan, C. Wu, Y. Jiao, A. Deng, C. Yan, J. Huang, S. Wu, W. Chen, T. Lei, P. Xu, W. He, J. Xiong, *Small* **2018**, *14*, 1802477.

[27] X. Pei, H. Jiao, H. Fu, X. Yin, D. Luo, S. Long, W. Gong, L. Zhang, *ACS Appl. Mater. Interfaces* **2020**, *12*, 51459–51467.

[28] J. Xu, R. Li, R. Zeng, X. Yan, Q. Zhao, J. Ba, W. Luo, D. Meng, *ACS Appl. Mater. Interfaces* **2020**, *12*, 38106-38112.

[29] a) X. Wang, M. Chen, X. Chen, R. Lin, H. Zhu, C. Huang, W. Yang, Y. Tan, S. Wang, Z. Du, Y. Ding, *J. Catal.* **2020**, *383*, 254-263; b) J. Sun, J. Yu, Q. Ma, F. Meng, X. Wei, Y. Sun, N. Tsubaki, *Sci. Adv.* **2018**, *4*, eaau3275.

[30] F. Liu, N. Yan, G. Zhu, Z. Liu, S. Ma, G. Xiang, S. Wang, X. Liu, W. Wang, *New J. Chem.* **2021**.

[31] Y. Sagara, A. K. Hara, W. Pavlicek, A. C. Silva, R. G. Paden, Q. Wu, *Am. J. Roentgenol.* **2010**, *195*, 713-719.

[32] M. Yu, Z. Wang, J. Liu, F. Sun, P. Yang, J. Qiu, *Nano Energy* **2019**, *63*, 103880.

[33] a) P. Hohenberg, W. Kohn, *Phys. Rev.* **1964**, *136*, B864-B871; b) G. Kresse, J. Furthmüller, *Phys. Rev. B* **1996**, *54*, 11169-11186; c) G. Kresse, J. Furthmüller, *Comput. Mater. Sci.* **1996**, *6*, 15-50; d) G. Kresse, J. Hafner, *Phys. Rev. B* **1994**, *49*, 14251-14269.

[34] P. E. Blöchl, *Phys. Rev. B* **1994**, *50*, 17953-17979.

[35] J. P. Perdew, K. Burke, M. Ernzerhof, *Phys. Rev. Lett.* **1996**, *77*, 3865-3868.

[36] H. J. Monkhorst, J. D. Pack, *Phys. Rev. B* **1976**, *13*, 5188-5192.

[37] J. K. Nørskov, J. Rossmeisl, A. Logadottir, L. Lindqvist, J. R. Kitchin, T. Bligaard, H. Jónsson, *J. Phys. Chem. B* **2004**, *108*, 17886-17892.

[38] a) G.-L. Chai, Z. Hou, D.-J. Shu, T. Ikeda, K. Terakura, *J. Am. Chem. Soc.* **2014**, *136*, 13629-13640; b) G.-L. Chai, K. Qiu, M. Qiao, M.-M. Titirici, C. Shang, Z. Guo, *Energy Environ. Sci.* **2017**, *10*, 1186-1195; c) G.-L. Chai, Z.-X. Guo, *Chem. Sci.* **2016**, *7*, 1268-1275.

TOC figure

A facile *in-situ* growth of blackberry-shaped Pt nanocrystals on Cu foams as self-standing HER electrode was presented. The optimized hydrogen adsorption free energy (ΔG_{*H}) and robust interaction between active materials and current collectors induced by charge density exchange ensure high efficiency and durability for HER in neutral media under technologically relevant high current densities.